Nanoscale

PAPER

View Article Online
View Journal | View Issue

Cite this: *Nanoscale*, 2024, **16**, 2373

Graphene quantum dot-mediated anchoring of highly dispersed bismuth nanoparticles on porous graphene for enhanced electrocatalytic CO_2 reduction to formate†

Yi Cheng,[a,b] Ruizhe Yang,[a,b] Lu Xia,[c] Xiaoli Zhao,*[d] Yuwei Tan,[a,b] Ming Sun,[a,b] Suming Li,[a,b] Fei Li*[e] and Ming Huang *[a,b]

The electrocatalytic reduction of CO_2 to produce formic acid is gaining prominence as a critical technology in the pursuit of carbon neutrality. Nonetheless, it remains challenging to attain both substantial formic acid production and high stability across a wide voltage range, particularly when utilizing bismuth-based catalysts. Herein, we present a novel graphene quantum dot-mediated synthetic strategy to achieve the uniform deposition of highly dispersed bismuth nanoparticles on porous graphene. This innovative design achieves an elevated faradaic efficiency for formate of 87.0% at –1.11 V *vs.* RHE with high current density and long-term stability. When employing a flow cell, a maximum $FE_{formate}$ of 80.0% was attained with a total current density of 156.5 mA cm^{-2}. The exceptional catalytic properties can be primarily attributed to the use of porous graphene as the support and the auxiliary contribution of graphene quantum dots, which enhance the dispersion of bismuth nanoparticles. This improved dispersion, in turn, has a significantly positive impact on CO_2 activation and the generation of *HCOO intermediates to facilitate the formation of formate. This work presents a straightforward technique to create uniform metal nanoparticles on carbon materials for advancing various electrolytic applications.

Received 18th November 2023,
Accepted 21st December 2023

DOI: 10.1039/d3nr05853k

rsc.li/nanoscale

Introduction

The efficient conversion of the greenhouse gas CO_2 into value-added fuels or chemicals is a significant approach for addressing CO_2 emissions while simultaneously mitigating the increasing scarcity of non-renewable fossil fuels.[1–10] Currently, the electrocatalytic CO_2 reduction reaction (CO_2RR) stands as one of the most promising avenues, owing to its mild reaction conditions and high energy efficiency. However, its practical realization and implementation pose a formidable challenge due to the inherent thermodynamic stability of CO_2 molecules and the multitude of reaction pathways for CO_2 reduction, which limit reaction selectivity. On the other hand, within the reaction pathway, the hydrogen evolution reaction (HER) in an aqueous electrolyte acts as a competing side reaction, making it challenging for the CO_2RR to generate the desired product.[11–17] Hence, there is a pressing demand to develop electrocatalysts with high efficiency for the CO_2RR that can enhance both the reaction rate and the selectivity toward the target product.

Among the products resulting from the CO_2RR, formic acid or formate has garnered substantial interest due to its numerous potential applications and promising economic benefits. It can be utilized in formic acid fuel cells, hydrogen storage, and as a raw material in various industrial processes.[18–23] In recent decades, researchers have explored various metal-based catalysts like Pb, In, Cd, Sn, and Co for the CO_2RR to generate formate in aqueous solutions. Unfortunately, these catalysts suffer from drawbacks such as high cost, poor selectivity, limited availability, and low durability, posing significant obstacles to their widespread practical applications.[24–26] In contrast, bismuth (Bi) is renowned for its excellent formate selectivity, low toxicity, and cost-effectiveness compared to pricier alternatives like Sn and In.[13,27–31] Nevertheless, certain

[a]*Institute of Fundamental and Frontier Sciences, University of Electronic Science and Technology of China, Chengdu 611731, China. E-mail: huangming@uestc.edu.cn*
[b]*Yangtze Delta Region Institute (Huzhou), University of Electronic Science and Technology of China, Huzhou 313001, China*
[c]*ICFO–Institut de Ciències Fotòniques, The Barcelona Institute of Science and Technology, Barcelona 08860, Spain*
[d]*School of Materials Science and Engineering, Xihua University, Chengdu, 610039, China. E-mail: zhaoxl@mail.xhu.edu.cn*
[e]*School of Materials and Energy, University of Electronic Science and Technology of China, Chengdu 611731, China. E-mail: feili@uestc.edu.cn*

†Electronic supplementary information (ESI) available: The experimental details and computational methods, XRD patterns, SEM images, XPS spectra, GC calibration curves, additional electrochemical test results, and DFT calculation results. See DOI: https://doi.org/10.1039/d3nr05853k

key issues persist, including low current density and poor catalytic stability arising from its chemically unstable and prone-to-agglomeration nature.[32] To address these issues, a crucial strategy involves immobilizing Bi on the support material to enhance stability and regulate spatial distribution. The strong interaction between the metal and support, termed metal–support interaction, provides substantial opportunities for enhancing electrocatalytic CO_2RR performance.

Various catalyst supports, including carbon materials, oxides, and nitrides, have been developed for the immobilization of metal nanoparticles.[33–36] Notably, porous graphene stands out as an ideal platform for metal catalysts owing to its expansive surface area, high conductivity, and chemical stability.[37,38] Confining metal nanoparticles onto graphene hinders particle aggregation by regulating their spatial distribution. The open structure of graphene layers facilitates the exposure of active sites, enhancing the adsorption and activation of CO_2 molecules for improved electroactivity and durability.[39,40] Additionally, the interface between metal nanoparticles and the support induces a noticeable redistribution of electrons. Combining Bi nanoparticles with a porous graphene support has the potential to improve both catalytic activity and stability in the electrochemical CO_2 reduction process. It is worth noting that the CO_2RR-to-formate activity is easily influenced by the particle size and mass loading of Bi on the graphene support. Therefore, there is a high desire, albeit a challenge, to devise a novel and efficient approach that can uniformly deposit Bi nanoparticles with controlled particle size.

Herein, we demonstrate a graphene quantum dot-assisted deposition strategy to synthesize uniformly loaded Bi nanoparticles on porous graphene (Bi NPs@PG). The abundant oxygenated groups and numerous defective sites of graphene quantum dots (GQDs) furnish porous graphene (PG) supports with high-density coordination sites. This facilitates the anchoring of Bi ions during the mixing process, resulting in the uniform deposition of Bi nanoparticles on PG after the pyrolysis process. As a result, the formate faradaic efficiency ($FE_{formate}$) for Bi NPs@PG demonstrates a notable value of 87.0% at −1.11 V (*vs.* RHE) with remarkable durability evidenced by long-term electrolysis. In addition, it exhibits high CO_2RR activity in a flow cell, achieving an $FE_{formate}$ of 80% and a partial current density of 156.5 mA cm^{-2}. Detailed theoretical calculations reveal that the interaction between Bi and PG leads to increased electron transfer toward *CO_2 and *HCOO. This establishes a favorable local coordination environment for CO_2 activation, reducing the energy barrier for *HCOO intermediate formation and ultimately enhancing formate formation. This study presents an accessible strategy to achieve uniform metal nanoparticle deposition on porous graphene and gain insights into the synergistic effect of metal and porous graphene in influencing the selectivity and activity in the CO_2RR.

Ming Huang

Ming Huang is currently a full professor at the Institute of Fundamental and Frontier Sciences, University of Electronic Science and Technology of China. He received his Ph.D. in the School of Materials Science and Engineering at the Ulsan National Institute of Science and Technology (South Korea) in 2018 under the supervision of Prof. Rodney S. Ruoff. Following his doctoral studies, he served as a postdoctoral research fellow at the Institute for Basic Science Center for Multidimensional Carbon Materials (2018–2019) and later at Nanyang Technological University (2019–2022). His research group focuses on nanomaterials (particularly carbon materials) and electrocatalysis.

Results and discussion

Fig. 1a and b show the preparation processes of the Bi nanoparticles on porous graphene (Bi NPs@PG) and Bi spheres on porous graphene (Bi SPs@PG) catalysts using PG as the carbon support. First, PG and GQDs were synthesized by a template-assisted chemical vapor deposition method and a refluxing method, respectively (detailed procedures are shown in the Experimental section in the ESI†). Characterization by X-ray diffraction (XRD), scanning electron microscopy (SEM), and transmission electron microscopy (TEM) validates the successful preparation of the materials (Fig. S1 and S2†). Subsequently, Bi NPs@PG and Bi SPs@PG were synthesized using the same method, differing only in the presence or absence of GQDs. In the presence of GQDs, the Bi cation initially forms a stable GQD–Bi coordination composite through complexation or crosslinking. The robust interaction between the Bi cation and O-containing groups in GQDs effectively prevents metal precursor aggregation. Therefore, achieving a highly dispersed metal precursor is a crucial step in the synthesis of uniform Bi NPs. Subsequently, the resulting metal complex is combined with PG *via* π–π interactions during a mixing process. The π-conjugated structure of GQDs ensures a strong interaction between the PG support and the GQD. Finally, Bi NPs@PG is obtained after pyrolysis in a reducing environment (Fig. 1b). Without GQDs, the Bi cations cannot be well dispersed on PG and, as a result, easily aggregate into nonuniform and irregular Bi spheres (Fig. 1a). The prominent peaks in the XRD patterns of the synthesized samples closely match the characteristic peaks of Bi (Fig. 1c). The lack of diffraction peaks for PG can be attributed to its inferior crystallinity in comparison with the pronounced intensity exhibited by the Bi nanoparticles. SEM and TEM images (Fig. 1d and e) reveal that Bi nanoparticles with sizes ranging from 30 to 40 nm are uniformly dispersed on the PG layer. The corresponding SEM images of commercial Bi and Bi SPs@PG are shown in

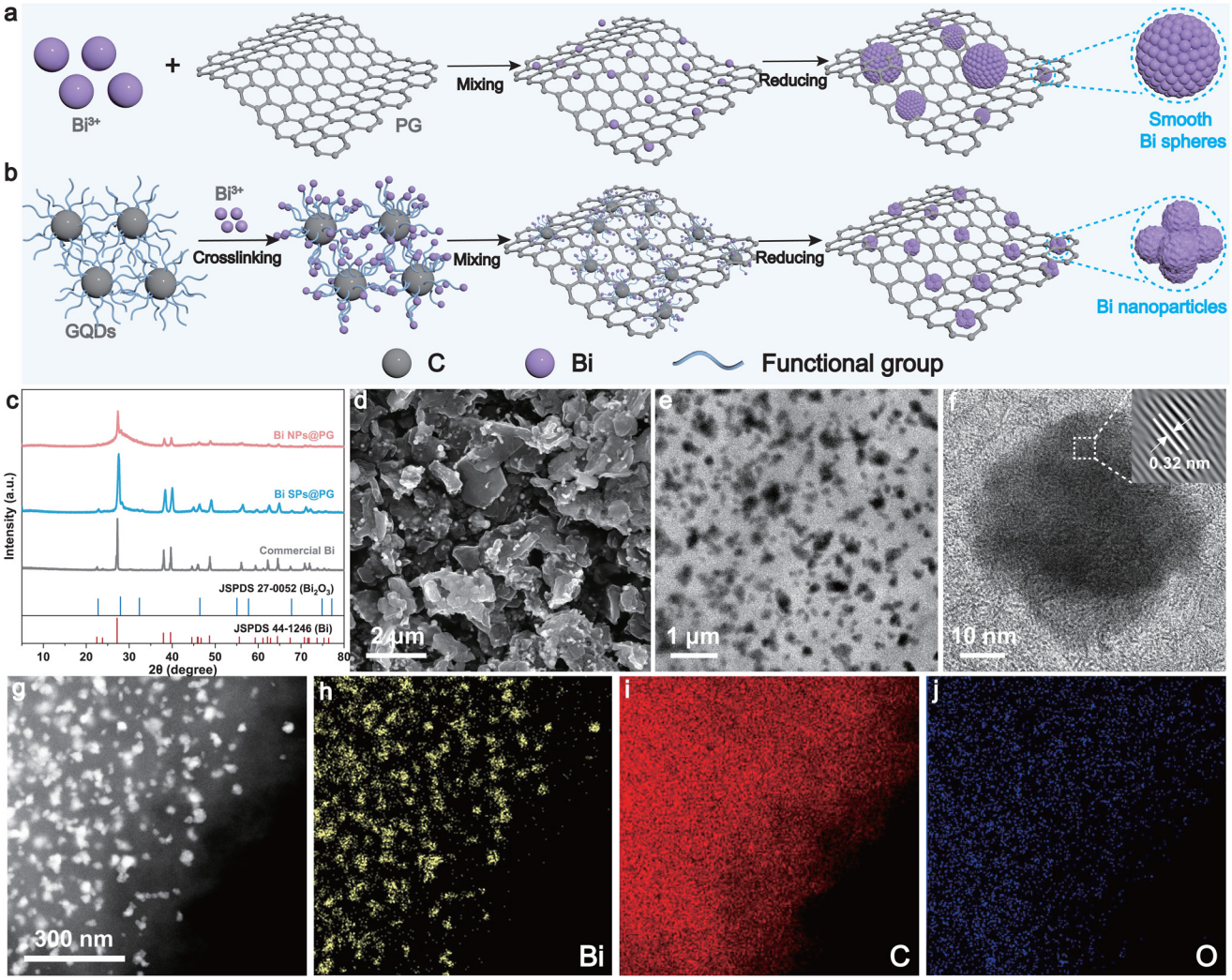

Fig. 1 Schematic illustration of the synthesis process of (a) Bi SP@PG (a) and (b) Bi NP@PG catalysts. (c) XRD patterns of Bi NPs@PG, Bi SPs@PG, and commercial Bi. (d–f) SEM, TEM, and HRTEM images of Bi NPs@PG. (g) STEM image of Bi NPs@PG, and (h–j) the corresponding EDS elemental mapping images.

Fig. S3.† The results indicate that commercial Bi exhibits a blocky morphology, while Bi SPs@PG adopts the shape of a smooth sphere with nonuniform sizes, revealing limitations in the surface area or active sites for subsequent CO_2 reduction reactions. The high-resolution transmission electron microscopy (HRTEM) image displays clear lattice fringes with an interplanar space of 0.32 nm, corresponding to the (012) plane of Bi and agreeing with the XRD findings (Fig. 1f). Additionally, the energy dispersive spectroscopy (EDS) mapping images (Fig. 1g–j) show a uniform distribution of Bi, C, and O within the Bi NPs@PG, affirming the consistent integration of Bi NPs within the graphene composite matrix.

X-ray photoelectron spectroscopy (XPS) measurement of the Bi NPs@PG reveals the presence of Bi, C, O, and N elements. In the Bi 4f spectrum, two peaks at 162.7 and 157.4 eV are assigned to Bi^0 $4f_{5/2}$ and Bi^0 $4f_{7/2}$, respectively. Additionally, the peaks located at 164.7 and 159.4 eV correspond to Bi^{3+} $4f_{5/2}$ and $4f_{7/2}$, respectively (Fig. S4a†).[41–43] The presence of Bi^{3+} peaks can be attributed to inevitable surface oxidation during sample preparation or characterization. The results from XRD and TEM indicate that the oxidation occurred only on the surface area, while the bulk material remains as metallic Bi. This surface oxidation was also observed in the Bi SP@PG sample (Fig. S5a†). It is noteworthy that the proportion of elemental metal Bi in Bi NPs@PG is higher than that in Bi SPs@PG. This is likely due to the former having a more uniform and smaller size, resulting in better encapsulation by PG and, thus, a slower rate of oxidation. The high-resolution C 1s spectrum exhibits three decoupled peaks corresponding to C–C (284.8 eV), C–N (285.9 eV), and C═O (288.1 eV), respectively (Fig. S4b†).[44,45] The prevalence of sp^2-bonded carbon atoms indicates a relatively high degree of carbonization for Bi NPs@PG, suggesting excellent conductivity for the catalysts. Peaks at 530.7 eV and 533.4 eV in the O 1s spectrum are ascribed to the Bi–O bonds and chemisorbed oxygen or OH species, respectively (Fig. S4c†).[11,46–48] The N 1s XPS spectrum

(Fig. S4d†) of Bi NPs@PG is fitted into three typical peaks corresponding to graphitic N (402.6 eV), pyrrolic N (400.7 eV), and pyridinic N (399.2 eV).[49] The XPS results above indicate the successful incorporation of Bi nanoparticles into the porous graphene support, leading to a rearrangement of electrons at the interface. This could further enhance the conductivity and activity of the catalyst. In addition, the high-resolution C 1s, O 1s and N 1s spectra of Bi SPs@PG are shown in Fig. S5.†

The electrocatalytic CO_2 reduction performance was assessed in a gastight two-compartment H-cell using 0.1 M $KHCO_3$ (CO_2-saturated) as the electrolyte. Linear sweep voltammetry (LSV) curves were recorded at a scan rate of 5 mV s^{-1} (Fig. 2a). The current density of the Bi NPs@PG, characterized by the lowest onset potential, sharply increases under a CO_2 flow, suggesting its superior CO_2 reduction activity in comparison with Bi SPs@PG and commercial Bi catalysts. To assess the CO_2 reduction efficiency at different potentials, we conducted a chronoamperometry test in a potential range of −0.83 to −1.19 V *vs.* RHE (Fig. S6†). Gaseous and liquid products were periodically analyzed using gas chromatography and ion chromatography, respectively (Fig. S7 and S8†). The faradaic efficiencies of Bi NPs@PG, Bi SPs@PG, and commercial Bi are presented in Fig. 2b and Fig. S9.† Notably, formate predominated as the product for Bi NPs@PG, accompanied by small amounts of CO and H_2 (Fig. S10†), demonstrating the highest faradaic efficiency of formate ($FE_{formate}$) of 87.0% at −1.11 V (*vs.* RHE) (Fig. 2b). This performance surpasses that of Bi SPs@PG (79.8%), commercial Bi (38.6%) and PG (<10%, Fig. S11†). Additionally, the $FE_{formate}$ remains >80% across a wide potential window (from −0.97 to −1.15 V *vs.* RHE) for Bi NPs@PG. The improved CO_2RR activity can be attributed to the introduction of GQDs, which offer numerous anchoring sites for Bi cations. GQDs combine with Bi cations through many functional groups, thereby facilitating the uniform deposition of Bi nanoparticles on the porous graphene support, resulting in more accessible sites for the CO_2RR. The partial

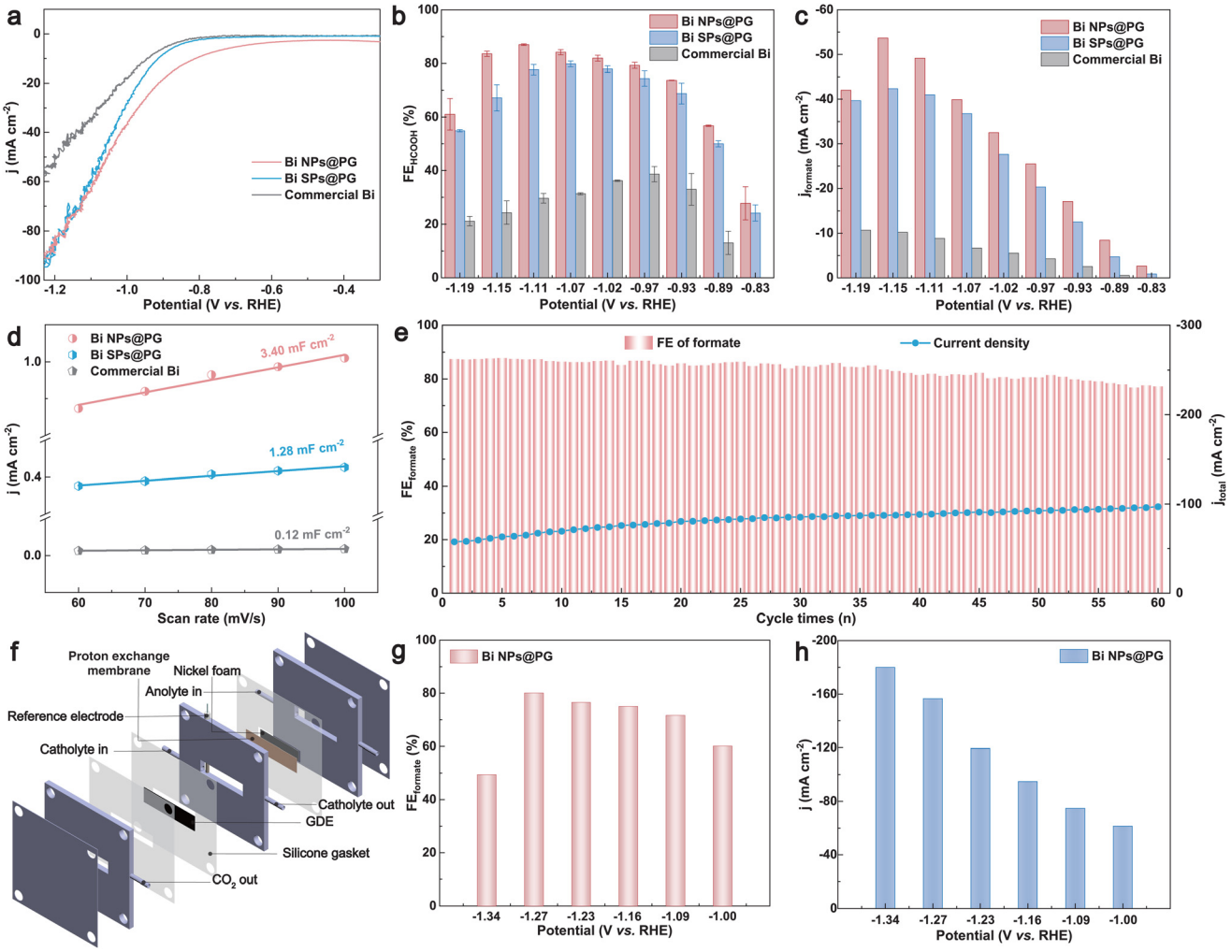

Fig. 2 (a) Linear sweep voltammetric (LSV) curves of Bi NPs@PG, Bi SPs@PG, and commercial Bi in CO_2-saturated 0.1 M $KHCO_3$. (b) Comparison of $FE_{formate}$ for the prepared catalysts. (c) Corresponding partial current density of formate for the prepared catalysts. (d) Electrochemically active surface areas (ECSAs) of the prepared catalysts. (e) Long-term stability test for Bi NPs@PG at −1.11 V *vs.* RHE. (f) Schematic illustration of the flow cell. (g and h) $FE_{formate}$ and the corresponding partial current density of formate for Bi NPs@PG measured in a flow cell.

formate current density ($j_{formate}$) of these catalysts in the corresponding potential range is shown in Fig. 2c. Bi NPs@PG exhibits the highest $j_{formate}$ of 53.7 mA cm^{-2} at −1.15 V, surpassing those of Bi SPs@PG (42.3 mA cm^{-2}) and commercial Bi (10.2 mA cm^{-2}), consistent with the LSV results. Faradaic efficiencies and partial current densities of CO and H_2 for these catalysts are also evaluated and presented in Fig. S9.† The electrochemical double-layer capacitance (C_{dl}) was measured through cyclic voltammetry (CV) to assess the electrochemically active surface area (ECSA) (Fig. S12†). As depicted in Fig. 2d, the C_{dl} value of the Bi NP@PG catalyst is 3.40 mF cm^{-2}, exceeding that of the other two catalysts. This is attributed to the uniform Bi NPs providing a large number of catalytically active sites, indicating their intrinsically superior catalytic activity for CO_2 reduction. Additionally, the stability of Bi NPs@PG was determined through long-term electrolysis at −1.11 V. After 60 cycles of electrolysis (each cycle lasting 1000 s), there was no significant decrease in $FE_{formate}$, demonstrating the high stability of Bi NPs@PG (Fig. 2e). For comparison, the stability of Bi SPs@PG and commercial Bi was also measured under the same electrolysis conditions, revealing lower current densities and a rapid decay in $FE_{formate}$ (Fig. S13†). These results indicate that the introduction of GQDs during the synthesis of Bi NPs@PG promotes the uniform deposition of Bi NPs and thus improves the catalyst stability. To address the low solubility limitation of CO_2 in an H-cell and showcase the feasibility of the CO_2RR for high-current-density practical application, the performance of Bi NPs@PG was further evaluated in a flow cell system using 0.5 M $KHCO_3$ as the cathode electrolyte (Fig. 2f). With testing conducted at potentials ranging from −1.00 V to −1.34 V (Fig. S14†), a peak $FE_{formate}$ of 80% was achieved at −1.27 V (Fig. 2g) with a total current density of 156.5 mA cm^{-2} (Fig. 2h), significantly exceeding the values obtained in the H-cell setup. At −1.34 V, an additional current increment was observed, highlighting the exceptional electrocatalytic performance of Bi NPs@PG in the CO_2RR process.

To probe the reaction intermediates and elucidate the reaction pathways of the CO_2RR to formate, *in situ* attenuated total reflection surface enhanced infrared absorption spectroscopy (ATR-SEIRAS) was performed during the electrolysis process at potentials ranging from 0.10 V to −1.90 V *vs.* RHE. As shown in Fig. 3a and c, the peaks at 1059 cm^{-1} and 1108 cm^{-1} are attributed to CO_3^{2-} species.[50] A peak observed at approximately 1645 cm^{-1} is assigned to the in-plane bending of water molecules. The band centers at 1239 cm^{-1} and 1274 cm^{-1} in the spectra of the two samples were assigned to the formation of $*CO_2^-$, ascribing to the CO_2 activation on the surface of the catalyst.[51] Two peaks located at ~1390 cm^{-1} and ~1580 cm^{-1} are attributed to the *HCOO species (vibration of O–C–O in

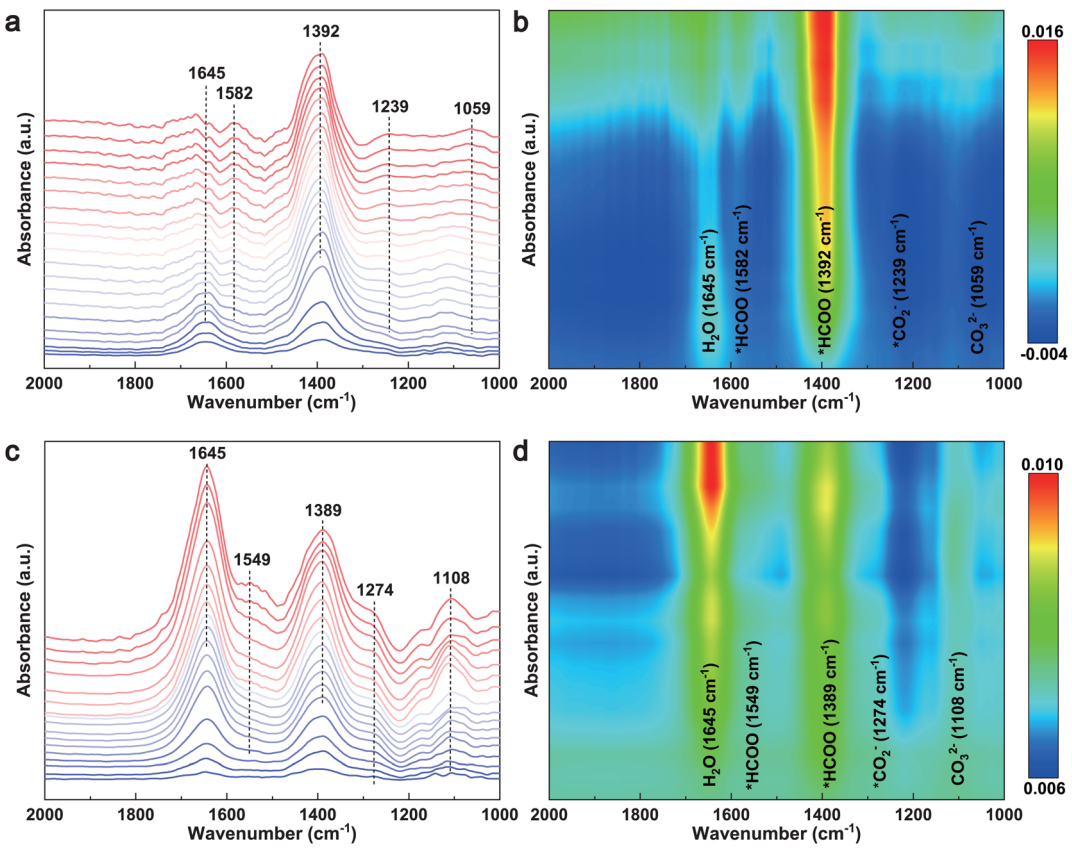

Fig. 3 *In situ* ATR-SEIRAS spectra of (a and b) Bi NPs@PG and (c and d) Bi SPs@PG in CO_2-saturated 0.1 M $KHCO_3$ solution from 0.1 V to −1.9 V *vs.* RHE.

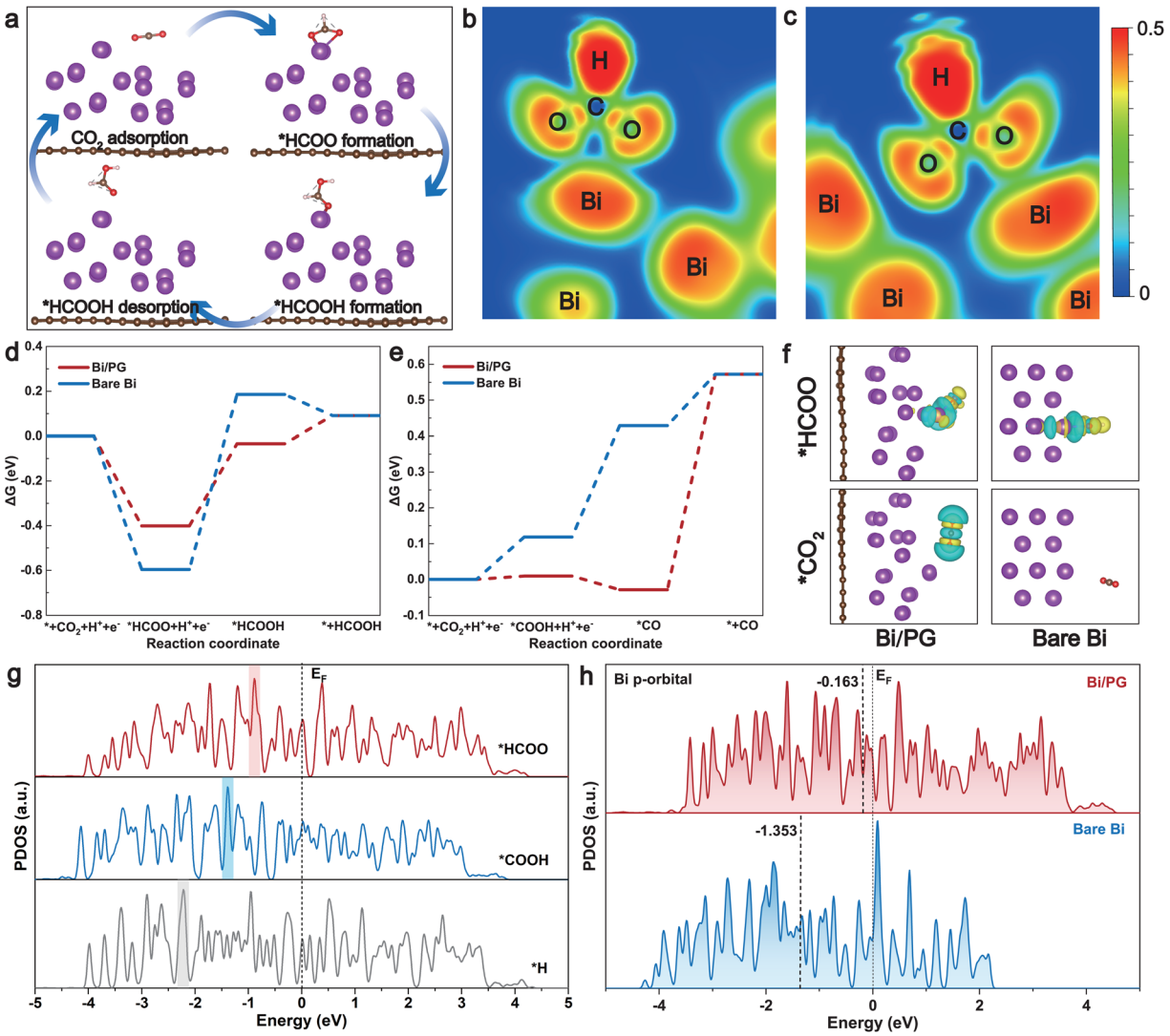

Fig. 4 (a) Reaction processes illustrating electrolytic CO_2 reduction to formate over the Bi/PG catalyst. (b and c) Electronic localization function (ELF) of *HCOO on Bi/PG and bare Bi surfaces. Gibbs free-energy diagrams for CO_2 reduction to (d) HCOOH and (e) CO on Bi/PG and bare Bi catalysts. (f) Side views of charge difference diagrams displaying the optimized adsorption configurations of *HCOO and $*CO_2$ on Bi/PG and bare Bi catalysts. The isosurface level sets to 0.002 e $Å^{-3}$, where charge depletion and accumulation are depicted by cyan and yellow, respectively. (g) Projected density of states (PDOS) for Bi p orbitals with adsorbed *HCOO, *COOH and *H in Bi/PG. The positions of the highest peak (E_p) of active site DOS with *HCOO, COOH*, or H* are highlighted with red, blue, and gray shading, respectively. (h) PDOS for Bi p-orbitals in Bi/PG and bare Bi catalysts. The dark dashed lines indicate the d-band center, and the Fermi level is set as zero.

formic acid).[52–54] The intensity of these two peaks increases with the applied potentials, indicating the gradual generation and accumulation of *HCOO during formate formation. These results reveal that $*CO_2^-$ and *HCOO are the key reaction intermediates, providing further insights into the reaction pathways of the formation of formate during the CO_2RR. It is worth noting that the intensity of *HCOO over Bi NPs@PG was significantly higher than that over Bi SPs@PG, indicating heightened activity and selectivity for formate formation.[55] These pieces of evidence suggest that the uniform deposition of Bi NPs on PG significantly promotes the activation of CO_2 molecules and enhances the generation of the key reaction intermediate (*HCOO), leading to improved CO_2 performance.

Density functional theory (DFT) calculations were further applied to simulate and compare the CO_2RR pathways on both bare and PG-supported Bi surfaces (see details in the Method section in the ESI†). Referring to the experimental data, various adsorption models were generated through structure optimization to simulate the CO_2RR process on the surface of Bi NPs@PG and commercial Bi. We constructed representative Bi/PG and bare Bi models, which are shown in Fig. S15 and S16,† highlighting the distinction between the cases with and without PG. The adsorption energy of CO_2 on the surface of Bi/PG is lower (more negative) than that on bare Bi. This suggests that the PG substrate enhances the adsorption of CO_2, thereby promoting its activation. The adsorption energy of *HCOO on

Bi/PG is also lower than that on the bare Bi surface (Fig. S15†). In light of the aforementioned results, the proposed reaction pathway for the CO_2RR to formic acid/formate on the catalyst surface is depicted in Fig. 4a. It underscores that the formation of the *HCOO intermediate is deemed the rate-determining step critical to the activity of formate. Electron localization function (ELF) maps clearly demonstrate that PG, as the substrate, significantly enhances the interaction of the *HCOO intermediate with Bi atoms (Fig. 4b and c).[11,56] In addition, the Gibbs free-energy diagrams for the CO_2RR on the two catalyst surfaces were constructed (Fig. 4d and e and Table S1†). As shown in Fig. 4d, the initial protonation of CO_2 to form *HCOO is exothermic on both the catalyst surfaces. In the second step, the free-energy change (ΔG) for further protonation of *HCOO to form *HCOOH on Bi/PG (0.37 eV) is much lower than that on bare Bi (0.78 eV). In addition, the Gibbs free-energy diagrams for competitive reaction pathways to generate CO and H_2 are also considered. The ΔG values for the formation of CO and H_2 are 0.59 and 4.97 eV on the Bi/PG surface, respectively, showing much larger energy barriers compared to the formation of HCOOH (Fig. 4e and Fig. S17†). It is evident from the calculations that Bi/PG is more favored for HCOOH formation, indicating that the introduction of PG promotes the reduction of CO_2 to HCOOH. The charge difference diagrams of the optimized adsorption configurations of *HCOO and *CO_2 on the two catalyst surfaces are displayed in Fig. 4f, Fig. S18 and S19.† Compared to the bare Bi surface, the electron accumulation at the interface where *HCOO and *CO_2 are absorbed is more significant on Bi/PG, enhancing the CO_2 reduction to formate.[57] The binding strength of various reaction intermediates could be deduced by comparing the projected density of states (PDOS) of the active Bi site with adsorbates (Fig. 4g). It has been reported that the position of the highest peak (E_p) of active site DOS with adsorbates was closer to the Fermi level, the stronger the adsorption strength.[58] In the model of Bi/PG, the E_p of *HCOO is closest to the Fermi level (E_f) compared to that of *COOH and *H, indicating the lowest filling of anti-bonding states and, consequently, stronger adsorbate binding.[59,60] In addition, the d-band center of Bi/PG (−0.163 eV) upshifts significantly compared to bare Bi (−1.353 eV) in the Bi p-orbital, following the general rule that a higher d-band center leads to a more reactive active site (lower transition state energy) (Fig. 4h),[12,61–63] which is also applicable to the Bi s-orbital and d-orbital (Fig. S20†). These results suggest that utilizing PG as the substrate modifies the electronic structure of Bi metal, boosting its intrinsic activity. The collaboration in the Bi NP@PG catalyst not only disperses and stabilizes Bi NPs but also promotes the formation of the *HCOO intermediate, thereby enhancing CO_2RR activity toward formate.

Conclusions

In summary, we established a cost-effective and straightforward synthesis route by leveraging graphene quantum dots to efficiently anchor Bi nanoparticles on porous graphene. The designed catalyst demonstrates remarkable efficiency in the electrolytic CO_2RR to formate, achieving an $FE_{formate}$ of 87.0% and a formate current density of 49.2 mA cm^{-2} at −1.11 V *vs.* RHE. The performance remains impressive in a flow cell, showing an $FE_{formate}$ > 80% at a current density of 156.5 mA cm^{-2}. *In situ* ATR-SEIRAS and DFT calculations indicate that porous graphene modifies the electronic structure of Bi metal, enhancing CO_2 adsorption energy, lowering the energy barrier for *HCOO intermediate formation, and thereby increasing activity. This work provides insights for the rational design of carbon-supported metal catalysts for wide electrocatalytic applications.

Experimental section

The experimental details are given in the ESI.†

Author contributions

Ming Huang conceived the original concept and initiated the project. Yi Cheng carried out the experiments, data analysis, and wrote the draft manuscript. Ruizhe Yang, Lu Xia, Yuwei Tan, Ming Sun and Suming Li participated in material characterization and data analysis. Xiaoli Zhao, Fei Li and Ming Huang revised the manuscript. All authors discussed the results and commented on the manuscript.

Conflicts of interest

The authors declare no competing interests.

Acknowledgements

This work was supported by the National Natural Science Foundation of China (52373223 and 52202215), Sichuan Science and Technology Program (2023NSFSC0434 and 2023NSFSC0956), and the China Postdoctoral Science Foundation (2022M720652).

References

1 P. De Luna, C. Hahn, D. Higgins, S. A. Jaffer, T. F. Jaramillo and E. H. Sargent, *Science*, 2019, **364**, eaav3506.
2 J. Zhu, J. Li, R. Lu, R. Yu, S. Zhao, C. Li, L. Lv, L. Xia, X. Chen, W. Cai, J. Meng, W. Zhang, X. Pan, X. Hong, Y. Dai, Y. Mao, J. Li, L. Zhou, G. He, Q. Pang, Y. Zhao, C. Xia, Z. Wang, L. Dai and L. Mai, *Nat. Commun.*, 2023, **14**, 4670.
3 O. S. Bushuyev, P. De Luna, C. T. Dinh, L. Tao, G. Saur, J. van de Lagemaat, S. O. Kelley and E. H. Sargent, *Joule*, 2018, **2**, 825–832.

4 B. Deng, M. Huang, X. Zhao, S. Mou and F. Dong, *ACS Catal.*, 2021, **12**, 331–362.
5 X. Wang, P. Ou, J. Wicks, Y. Xie, Y. Wang, J. Li, J. Tam, D. Ren, J. Y. Howe, Z. Wang, A. Ozden, Y. Z. Finfrock, Y. Xu, Y. Li, A. S. Rasouli, K. Bertens, A. H. Ip, M. Graetzel, D. Sinton and E. H. Sargent, *Nat. Commun.*, 2021, **12**, 3387.
6 Z. Li, X. Qi, J. Wang, Z. Zhu, J. Jiang, X. Niu, A. Cabot, J. S. Chen and R. Wu, *SusMat*, 2023, **3**, 498–509.
7 T. Tang, Z. Wang and J. Guan, *Exploration*, 2023, **3**, 20230011.
8 J. H. Cho, J. Ma and S. Y. Kim, *Exploration*, 2023, **3**, 20230001.
9 Y. Zhai, P. Han, Q. Yun, Y. Ge, X. Zhang, Y. Chen and H. Zhang, *eScience*, 2022, **2**, 467–485.
10 A. Conte, M. Baron, S. Bonacchi, S. Antonello and A. Aliprandi, *Nanoscale*, 2023, **15**, 3693–3703.
11 M. Huang, B. Deng, X. Zhao, Z. Zhang, F. Li, K. Li, Z. Cui, L. Kong, J. Lu, F. Dong, L. Zhang and P. Chen, *ACS Nano*, 2022, **16**, 2110–2119.
12 G. Wen, D. U. Lee, B. Ren, F. M. Hassan, G. Jiang, Z. P. Cano, J. Gostick, E. Croiset, Z. Bai, L. Yang and Z. Chen, *Adv. Energy Mater.*, 2018, **8**, 1802427.
13 N. Han, P. Ding, L. He, Y. Li and Y. Li, *Adv. Energy Mater.*, 2019, **10**, 1902338.
14 Y. Zhang, V. Sethuraman, R. Michalsky and A. A. Peterson, *ACS Catal.*, 2014, **4**, 3742–3748.
15 Q. Li, Y. Zhang, L. Shi, M. Wu, Y. Ouyang and J. Wang, *InfoMat*, 2021, **3**, 1285–1294.
16 F. Chen, Z. Yao, Z. Lyu, J. Fu, X. Zhang and J. Hu, *eScience*, 2023, DOI: **10.1016/j.esci.2023.100172**.
17 J. Yin, J. Jin, Z. Yin, L. Zhu, X. Du, Y. Peng, P. Xi, C. Yan and S. Sun, *Nat. Commun.*, 2023, **14**, 1724.
18 L. C. Pardo Pérez, D. Teschner, E. Willinger, A. Guiet, M. Driess, P. Strasser and A. Fischer, *Adv. Funct. Mater.*, 2021, **31**, 2103601.
19 L. Jia, M. Sun, J. Xu, X. Zhao, R. Zhou, B. Pan, L. Wang, N. Han, B. Huang and Y. Li, *Angew. Chem., Int. Ed.*, 2021, **60**, 21741–21745.
20 G. Wang, F. Wang, P. Deng, J. Li, C. Wang, Y. Hua, Y. Shen and X. Tian, *Mater. Rep.: Energy*, 2023, **3**, 100181.
21 X. Liu, K. Zhang, Y. Sun, S. Zhang, Z. Qiu, T. Song, J. Xie, Y. Wu and Y. Chen, *SusMat*, 2023, **3**, 235–247.
22 L. Liu, X. Li, Y. Cai, H. Du, F. Liu, J. Zhang, J. Fu and W. Zhu, *Nanoscale*, 2022, **14**, 13679–13688.
23 B. Miao, W. Fang, B. Sun, F. Li, X. Wang, B. Xia and Y. Chen, *Chin. J. Struct. Chem.*, 2023, **42**, 100095.
24 F. Yang, A. O. Elnabawy, R. Schimmenti, P. Song, J. Wang, Z. Peng, S. Yao, R. Deng, S. Song, Y. Lin, M. Mavrikakis and W. Xu, *Nat. Commun.*, 2020, **11**, 1088.
25 L. Dai, Q. Qin, P. Wang, X. Zhao, C. Hu, P. Liu, R. Qin, M. Chen, D. Ou, C. Xu, S. Mo, B. Wu, G. Fu, P. Zhang and N. Zheng, *Sci. Adv.*, 2017, **3**, e1701069.
26 T. Wang, W.-S. Fang, Y. Liu, F. Li, P. Chen and Y. Chen, *J. Energy Chem.*, 2022, **70**, 407–413.
27 E. Zhang, T. Wang, K. Yu, J. Liu, W. Chen, A. Li, H. Rong, R. Lin, S. Ji, X. Zheng, Y. Wang, L. Zheng, C. Chen, D. Wang, J. Zhang and Y. Li, *J. Am. Chem. Soc.*, 2019, **141**, 16569–16573.
28 X. Liang, N. Tian, S. Hu, Z. Zhou and S. Sun, *Mater. Rep.: Energy*, 2023, **3**, 100191.
29 Y. Zhang, Y. Chen, R. Liu, X. Wang, H. Liu, Y. Zhu, Q. Qian, Y. Feng, M. Cheng and G. Zhang, *InfoMat*, 2022, **5**, e12375.
30 J. Yin, Z. Yin, J. Jin, M. Sun, B. Huang, H. Lin, Z. Ma, M. Muzzio, M. Shen, C. Yu, H. Zhang, Y. Peng, P. Xi, C.-H. Yan and S. Sun, *J. Am. Chem. Soc.*, 2021, **143**, 15335–15343.
31 S. Wu, M. Tian, Y. Hu, N. Zhang, W. Shen, J. Li, L. Guo, P. Da, P. Xi and C.-H. Yan, *Inorg. Chem.*, 2023, **62**, 4088–4096.
32 Q. Gong, P. Ding, M. Xu, X. Zhu, M. Wang, J. Deng, Q. Ma, N. Han, Y. Zhu, J. Lu, Z. Feng, Y. Li, W. Zhou and Y. Li, *Nat. Commun.*, 2019, **10**, 2807.
33 Y. Xu, X. Shi, R. Hua, R. Zhang, Y. Yao, B. Zhao, T. Liu, J. Zheng and G. Lu, *Appl. Catal., B*, 2020, **260**, 118142.
34 R. Ryoo, J. Kim, C. Jo, S. W. Han, J. Kim, H. Park, J. Han, H. S. Shin and J. W. Shin, *Nature*, 2020, **585**, 221–224.
35 Z. Wu, C. Li, Z. Li, K. Feng, M. Cai, D. Zhang, S. Wang, M. Chu, C. Zhang, J. Shen, Z. Huang, Y. Xiao, G. A. Ozin, X. Zhang and L. He, *ACS Nano*, 2021, **15**, 5696–5705.
36 P. Zhou, N. Li, Y. Chao, W. Zhang, F. Lv, K. Wang, W. Yang, P. Gao and S. Guo, *Angew. Chem., Int. Ed.*, 2019, **58**, 14184–14188.
37 X. Jing, Z. Zhu, L. Chen, D. Liu, H. Huang, W. Tian and A. Yin, *ACS Appl. Mater. Interfaces*, 2023, **15**, 20317–20324.
38 C. Rogers, W. S. Perkins, G. Veber, T. E. Williams, R. R. Cloke and F. R. Fischer, *J. Am. Chem. Soc.*, 2017, **139**, 4052–4061.
39 P. Su, W. Pei, X. Wang, Y. Ma, Q. Jiang, J. Liang, S. Zhou, J. Zhao, J. Liu and G. Q. Lu, *Angew. Chem., Int. Ed.*, 2021, **60**, 16044–16050.
40 J. Wang, X. Huang, S. Xi, J. M. Lee, C. Wang, Y. Du and X. Wang, *Angew. Chem., Int. Ed.*, 2019, **58**, 13532–13539.
41 P. Xiong, P. Bai, A. Li, B. Li, M. Cheng, Y. Chen, S. Huang, Q. Jiang, X. H. Bu and Y. Xu, *Adv. Mater.*, 2019, **31**, 1904771.
42 Y. Liang, N. Song, Z. Zhang, W. Chen, J. Feng, B. Xi and S. Xiong, *Adv. Mater.*, 2022, **34**, e2202673.
43 G. Li, W. Qiu, W. Gao, Y. Zhu, X. Zhang, H. Li, Y. Zhang, X. Wang and Z. Chen, *Adv. Funct. Mater.*, 2022, **32**, 2202853.
44 K. Zhou, S. Wang, X. Guo, G. Zhong, Z. Liu, Y. Ma, H. Wang, Y. Bao, D. Han and L. Niu, *Small*, 2022, **18**, e2105770.
45 Q. Zhang, J. Zhang, X. Wang, L. Li, Y. Li and W.-L. Dai, *ACS Catal.*, 2021, **11**, 6276–6289.
46 H. Wang, D. Wei, Y. He, H. Deng, B. Wu, L. Yan, H. Gang, Y. Cao, L. Jin and L. Zhang, *ACS Appl. Mater. Interfaces*, 2022, **14**, 13177–13185.
47 B. Pu, Y. Liu, J. Bai, X. Chu, X. Zhou, Y. Qing, Y. Wang, M. Zhang, Q. Ma, Z. Xu, B. Zhou and W. Yang, *ACS Nano*, 2022, **16**, 18746–18756.
48 P. Xiong, J. Wu, M. Zhou and Y. Xu, *ACS Nano*, 2020, **14**, 1018–1026.

49 J. Liu, S. Zhao, C. Li, M. Yang, Y. Yang, Y. Liu, Y. Lifshitz, S. Lee and Z. Kang, *Adv. Energy Mater.*, 2016, **6**, 1502039.
50 Y. Wang, S. Kattel, W. Gao, K. Li, P. Liu, J. G. Chen and H. Wang, *Nat. Commun.*, 2019, **10**, 1166.
51 Y. Liu, Z. X. Lou, X. Wu, B. Mei, J. Chen, J. Y. Zhao, J. Li, H. Y. Yuan, M. Zhu, S. Dai, C. Sun, P. F. Liu, Z. Jiang and H. G. Yang, *Adv. Mater.*, 2022, **34**, 2202568.
52 Z. Wu, H. Wu, W. Cai, Z. Wen, B. Jia, L. Wang, W. Jin and T. Ma, *Angew. Chem., Int. Ed.*, 2021, **60**, 12554–12559.
53 Y. Shi, Y. Ji, J. Long, Y. Liang, Y. Liu, Y. Yu, J. Xiao and B. Zhang, *Nat. Commun.*, 2020, **11**, 3415.
54 C. Cao, D. D. Ma, J. F. Gu, X. Xie, G. Zeng, X. Li, S. G. Han, Q. L. Zhu, X. T. Wu and Q. Xu, *Angew. Chem., Int. Ed.*, 2020, **59**, 15014–15020.
55 X. Zhao, M. Huang, B. Deng, K. Li, F. Li and F. Dong, *Chem. Eng. J.*, 2022, **437**, 135114.
56 Q. Cheng, M. Huang, L. Xiao, S. Mou, X. Zhao, Y. Xie, G. Jiang, X. Jiang and F. Dong, *ACS Catal.*, 2023, **13**, 4021–4029.
57 S. Liu, Y. Fan, Y. Wang, S. Jin, M. Hou, W. Zeng, K. Li, T. Jiang, L. Qin, Z. Yan, Z. Tao, X. Zheng, C. Shen, Z. Liu, T. Ahmad, K. Zhang and W. Chen, *Nano Lett.*, 2022, **22**, 9107–9114.
58 Y. Jiao, Y. Zheng, K. Davey and S. Qiao, *Nat. Energy*, 2016, **1**, 16130.
59 N. Han, Y. Wang, H. Yang, J. Deng, J. Wu, Y. Li and Y. Li, *Nat. Commun.*, 2018, **9**, 1320.
60 Y. Zhao, X. Liu, Z. Liu, X. Lin, J. Lan, Y. Zhang, Y. R. Lu, M. Peng, T. S. Chan and Y. Tan, *Nano Lett.*, 2021, **21**, 6907–6913.
61 Y. X. Duan, Y. T. Zhou, Z. Yu, D. X. Liu, Z. Wen, J. M. Yan and Q. Jiang, *Angew. Chem., Int. Ed.*, 2021, **60**, 8798–8802.
62 B. Hammer, J. K. Norskov, B. C. Gates and H. Knozinger, *Adv. Catal.*, 2000, **45**, 71–129.
63 G. Jia, Y. Wang, M. Sun, H. Zhang, L. Li, Y. Shi, L. Zhang, X. Cui, T. W. B. Lo, B. Huang and J. C. Yu, *J. Am. Chem. Soc.*, 2023, **145**, 14133–14142.